



Ultra-small nanocluster mediated synthesis of Nd³⁺-doped core-shell nanocrystals with emission in the second near-infrared window for multimodal imaging of tumor vasculature

Feng Ren^a, Lihua Ding^a, Hanghang Liu^a, Qian Huang^a, Hao Zhang^a, Lijuan Zhang^b, Jianfeng Zeng^a, Qiao Sun^a, Zhen Li^{a,b,*}, Mingyuan Gao^a

^a Center for Molecular Imaging and Nuclear Medicine, State Key Laboratory of Radiation Medicine and Protection, School for Radiological and Interdisciplinary Sciences (RAD-X), Soochow University, Collaborative Innovation Center of Radiation Medicine of Jiangsu Higher Education Institutions, Suzhou 215123, China

^b Institute for Superconducting and Electronic Materials, Australian Institute for Innovative Materials, University of Wollongong, Wollongong, NSW 2500, Australia

ARTICLE INFO

Article history:

Received 3 January 2018

Received in revised form

27 April 2018

Accepted 14 May 2018

Available online 15 May 2018

Keywords:

Nd³⁺-doped core-shell nanocrystals

NIR II fluorescence imaging

Magnetic resonance imaging

Computed tomography imaging

Tumor vasculature

ABSTRACT

In-vivo intravital short wavelength infrared (SWIR, 1000–2300 nm) fluorescence imaging has attracted considerable attention in the imaging of tumor vasculature due to its low background, high sensitivity, and deep penetration. It can noninvasively provide dynamic feedback on the tumorigenesis, growth, necrosis and metastasis. Herein, monodisperse Nd³⁺-doped core-shell downconversion luminescent nanocrystals with strong emission in the second near-infrared (NIR II) window, strong temperature-dependent paramagnetism and fast attenuation to X-rays were prepared from ultra-small nanoclusters. The use of nanoclusters resulted in very uniform bright nanocrystals with a relative quantum yield comparable to the standard dye IR-26. These bright NIR nanocrystals were modified with 1,2-distearoyl-sn-glycero-3-phosphoethanolamine-*N*-[methoxy(polyethylene glycol)-2000] to endow with excellent water-solubility, biocompatibility and a blood circulation half-life of 5.9 h. They were then successfully used to demonstrate the variation of tumor vasculature with tumor progression from tumorigenesis, growth, to necrosis in the subcutaneous breast tumor through the NIR II fluorescence imaging. They were also used as contrast agent of magnetic resonance imaging (MRI) and X-ray computed tomography (CT) imaging of tumor to provide complementary anatomic structure. Their great potential in NIR II imaging of tumor was further demonstrated with an orthotopic breast tumor. Their *in-vivo* biosafety was also investigated by hemanalysis and histological analyses.

© 2018 Elsevier Ltd. All rights reserved.

1. Introduction

Tumor vasculature has played significant roles in tumorigenesis, growth and metastasis. It not only serves as channels for supplying nutrients and oxygen during tumorigenesis and growth, but also acts as pathways for tumor metastasis [1,2]. The variation of tumor vasculature has been used for tumor staging, and considered as an

* Corresponding author. Center for Molecular Imaging and Nuclear Medicine, State Key Laboratory of Radiation Medicine and Protection, School for Radiological and Interdisciplinary Sciences (RAD-X), Soochow University, Collaborative Innovation Center of Radiation Medicine of Jiangsu Higher Education Institutions, Suzhou 215123, China.

E-mail address: zhenli@suda.edu.cn (Z. Li).

important prognostic indicator for evaluating tumor metastasis. For example, a tumor with dense vasculature has a higher incidence of metastasis than one with poor vasculature [1,3]. From perspective of diagnosis and treatment, tumor vasculature has been extensively used to deliver imaging agents and drugs through the enhanced penetration and retention (EPR) effect, which arises from its non-uniform, chaotic, and highly permeable features in comparison with a healthy vasculature [4,5]. It should be noted that the tumor vasculature is strongly dependent on the specific properties of tumor (e.g., tumor model, tumor size and tumor site) [6]. During tumor therapy, the variation of tumor vasculature can be used to evaluate the efficacy of treatment [7,8].

The above statements demonstrate the significance of tumor vasculature. It is crucial to monitor its formation and variation

through versatile molecular imaging techniques, which could provide significant guidance for tumor staging and therapy, and for evaluation of tumor metastasis. Currently available techniques for imaging of tumor vasculature include X-ray computed tomography (CT) and magnetic resonance angiography (MRA) due to their unlimited penetration depth and high spatial resolution [9,10]. They usually take long time to acquire high-quality images or process the images acquired [11], however. A complementary method is the newly developed intravital short-wavelength infrared (SWIR, 1000–2300 nm) fluorescence imaging, which can provide real-time dynamic feedback.

The SWIR fluorescence imaging has shown improvements in penetration and in overcoming tissue autofluorescence, with the rapid development of near-infrared fluorescent probes, especially those with emissions in the second near-infrared biological window (NIR II) from 1000 nm to 1700 nm [12–14]. A number of NIR II nanoprobes, such as single-walled carbon nanotubes (SWNTs) [15,16], Ag₂S and core-shell-shell InAs@CdSe@CdS quantum dots (QDs) [17–19], and small-molecular dyes [20–22], have been successfully applied for *in-vivo* imaging of vasculature, which suggests the great potential of NIR II fluorescence imaging in visualization of tumor vasculature.

Recently, lanthanide-doped nanocrystals (NCs) with down-conversion luminescence in the NIR II window have become a promising nanotheranostic agent due to their narrow band emission, deep penetration, long emission lifetime, excellent photostability, and low toxicity [23,24]. The lanthanide NCs sensitized by Yb³⁺ or Nd³⁺ ions are capable of generating narrow SWIR emission with a large Stokes shift [25–28]. For Yb³⁺ ion-sensitized rare-earth NCs, which are commonly excited by a continuous-wave 980 nm laser, the Yb³⁺ ions absorb the laser photon energy and then transfer it to activators (e.g., Er³⁺, Tm³⁺, and Ho³⁺ ions). Due to the fact that overheating caused by 980-nm irradiation could damage healthy tissues and reduce the depth of penetration [29], excitation at ~800 nm is favored due to the low absorption of biological tissue at this wavelength. In this context, Nd³⁺-based rare-earth NCs are more attractive, because Nd³⁺ ions can simultaneously serve as sensitizers and activators, whether they are in the form of dopants [30–32] or host matrix [33]. They can be excited at ~800 nm to produce narrow SWIR emissions at ~1050 nm (⁴F_{3/2} → ⁴I_{11/2}) and ~1300 nm (⁴F_{3/2} → ⁴I_{13/2}) for NIR II fluorescence imaging. Previous studies have demonstrated that Nd³⁺ ions were mainly used as dopants, and the optimal molar ratio for doping is around 5%, as more Nd³⁺ ions could cause a quenching effect and reduce the photoluminescence efficiency [34–36]. Most Nd³⁺-doped rare-earth NCs were applied for *in-vivo* NIR imaging with deep penetration [27,37,38], cancer theranostics [39,40], and monitoring of gastrointestinal drug-release [24].

From perspective of application, it is extremely important to construct core-shell nanostructure, e.g., Nd³⁺-doped core-shell rare-earth NCs, in order to improve their luminescence and attenuation to X-rays, and to introduce other properties such as magnetism. The core-shell rare-earth NCs have been usually prepared by a successive layer-by-layer (SLBL) approach [41–43] or by ripening-mediated epitaxial growth [44,45], in both of which small molecular precursors [e.g., lanthanide oleate (Ln-OA), lanthanide trifluoroacetate (Ln-TFA), and sodium trifluoroacetate (Na-TFA)], or the sacrificed nanoseeds were prepared at high temperature in advance. The reaction parameters during synthesis must be finely tuned in order to obtain monodisperse NCs, because the fast decomposition of molecular precursors at high temperature could result in a burst of nucleation, which is difficult to be separated from growth process and leads to a broad particle size distribution [46–48]. Therefore, development of robust approaches for fabrication of high-quality multifunctional core-shell NCs for imaging of

tumor vasculature is highly significant.

In this article, an ultra-small nanocluster mediated method was developed to prepare a series of Nd³⁺-doped core-shell NCs with uniform size and morphology, from NaYF₄, NaNdF₄ and NaGdF₄ nanoclusters, which serve as precursors for core, dopant and shell. Among the resultant core-shell NCs, NaYF₄:5%Nd@NaGdF₄ NCs exhibit the brightest luminescence in the NIR II window, strong temperature-dependent paramagnetism and fast attenuation towards X-rays. They were selected for NIR II imaging of breast tumor, which grew for different days after subcutaneous inoculation of 4T1 cells. The imaging results and the histological analyses clearly show the variation of tumor vasculature during the evolution of tumor from tumorigenesis, growth, to necrosis. Their potential in visualization of tumor vasculature by the NIR II fluorescence imaging was also demonstrated with an orthotopic breast tumor. They were also proved to be an excellent agent for MRI imaging and CT imaging of tumor.

2. Materials and methods

2.1. Materials

Gadolinium (III) chloride hexahydrate (GdCl₃·6H₂O, 99.9%), yttrium (III) chloride hexahydrate (YCl₃·6H₂O, 99.99%), neodymium (III) chloride hexahydrate (NdCl₃·6H₂O, 99.9%), sodium fluoride (NaF, 99.99%), oleic acid (OA, 85%) and 1-octadecene (ODE, 90%) were purchased from Aladdin Co. Ltd. Sodium hydroxide (NaOH, 96%) was obtained from Beijing Chemical Reagents Co. Ltd. 1,2-distearoyl-sn-glycero-3-phosphoethanolamine-*N*-[methoxy(polyethylene glycol)-2000] (DSPE-PEG₂₀₀₀) was purchased from Shang Hai Ponsure Biotech, Inc. All chemicals were used as received without further purification.

2.2. Preparation of nanocluster precursors and nanocrystals

2.2.1. Preparation of ultra-small lanthanide fluoride (NaLnF₄) nanoclusters as precursors

The liquid-solid-solution (LSS) strategy [49,50] was employed to prepare ultra-small lanthanide fluoride nanocluster precursors. In a typical synthesis, 1 mL yttrium (III) chloride hexahydrate aqueous solution (0.5 mol/L) and 4 mL sodium fluoride solution (0.5 mol/L) were added dropwise to a mixture of sodium hydroxide (1.2 g), ethanol (8 mL), deionized water (4 mL), and oleic acid (20 mL). The resultant solution was thoroughly stirred for 1 h at room temperature to form a yellowish solution, which was precipitated with ethanol to collect NaYF₄ nanoclusters. The obtained NaYF₄ nanoclusters were washed with ethanol several times, and then dispersed in 2 mL cyclohexane for further use.

The synthesis and purification of NaGdF₄ and NaNdF₄ nanoclusters are similar to NaYF₄ nanoclusters, except the replacement of YCl₃ with GdCl₃ or NdCl₃.

2.2.2. Synthesis of NaREF₄:5%Nd (RE = Gd, Y) NCs

NaREF₄ (RE = Gd, Y) nanoclusters were dispersed in 2 mL cyclohexane (0.25 mol/L) and then mixed with 6 mL oleic acid and 10 mL 1-octadecene in a 100 mL three-neck flask. The flask was purged with nitrogen at 70 °C for 30 min to fully remove the cyclohexane, and then heated to 280 °C at a rate of ~10 °C/min. After the mixture reacted for 30 min at 280 °C, 420 μL of NaNdF₄ nanocluster solution (0.0625 mol/L) was injected into the mixture and reacted for another 30 min. The reaction mixture was cooled to room temperature and centrifuged at 11000 rpm for 10 min, after which, the resultant precipitates were washed with absolute ethanol and then dispersed in chloroform.

2.2.3. Synthesis of NaREF₄:5%Nd@NaREF₄ (RE = Gd, Y) core-shell NCs

The precursors for growth of shell are NaGdF₄ or NaYF₄ nanoclusters, which were dispersed in 2 mL cyclohexane (0.25 mol/L) and then mixed with 6 mL oleic acid and 10 mL 1-octadecene. The core NCs (NaGdF₄:5%Nd or NaYF₄:5%Nd) were prepared from the NaLnF₄ nanoclusters as described previously. The reaction mixture of core NCs was cooled to 30 °C, and 0.5 mmol NaGdF₄ or NaYF₄ nanocluster solution was added. The flask was purged with nitrogen at 70 °C for 30 min to fully remove the cyclohexane, and the reaction solution was heated to 280 °C at a rate of ~10 °C/min and reacted for 1 h. After the reaction mixture was cooled to room temperature, it was centrifuged at 11000 rpm for 10 min to collect core-shell NCs, which were washed with absolute ethanol and finally dispersed in chloroform.

2.3. Modification of core-shell NaYF₄:5%Nd@NaGdF₄ NCs with phospholipids

A chloroform solution of oleic acid capped NaYF₄:5%Nd@NaGdF₄ core-shell NCs (0.5 mL, 0.05 mmol) was mixed with another chloroform solution of phospholipid (2 mL, 12.5 mg) in a screw-neck glass vial. The chloroform was slowly evaporated at room temperature for 24 h in a fume hood. The obtained film was heated at 75 °C for 5 min to completely remove the chloroform, and then dissolved in 5 mL Milli-Q water under sonication for 1 min and stirred vigorously for 10 min at 75 °C. The aqueous solution was transferred into a microtube and centrifuged at 20000 rpm for 10 min. After removal of the supernatant, 2 mL physiological saline (0.9 wt% NaCl) was added to dissolve the precipitates, and the solution was centrifuged at 5000 rpm for 5 min to remove the large aggregates. The resulting solution was filtered with a 0.22 μm membrane and stored at 5 °C for further use.

2.4. Characterization

TEM images were captured with a FEI Tecnai G20 transmission electron microscope operating at an acceleration voltage of 200 kV. The high-resolution TEM and high-angle annular dark field – scanning TEM (HAADF-STEM) images were collected with a JEOL JEM-2010F. The fluorescence spectra were recorded on a FLS980 spectrometer (Edinburgh Instruments, UK) equipped with 808-nm and 980-nm continuous-wave (CW) laser diodes (2 W), which served as the excitation sources. The hydrodynamic size was measured at 25 °C with a Malvern Zetasizer Nano ZS90 equipped with a solid state He–Ne laser ($\lambda = 633$ nm). The crystal structures of nanoparticles were characterized with a Shimadzu XRD-6000 X-ray diffractometer equipped with Cu K α 1 radiation ($\lambda = 0.15406$ nm).

2.5. Cytotoxicity assay

The standard MTT assay was performed to evaluate the cytotoxicity of core-shell NCs towards cancer cells. 4T1 cells (1×10^4 cells per well) were first seeded into 96-well plates and cultured for 24 h in a standard cell medium at 37 °C in 5% CO₂ atmosphere. Then, these cells were washed with PBS and incubated with DSPE-PEG₂₀₀₀ modified core-shell NaYF₄:5%Nd@NaGdF₄ NCs in different concentrations (6.25, 12.5, 25, 50, 100, 200, and 400 μg/mL) for 24 h. After that, the cells were washed with PBS, and 20 μL MTT [(3-(4,5-dimethylthiazol-2-yl)-2,5-diphenyltetrazolium bromide)] solution (5 mg/mL) was added and incubated with the cells for 4 h before the addition of 150 μL dimethyl sulfoxide (DMSO). The absorbance of each solution at 490 nm was measured by a microplate reader (Thermo, Varioskan Flash).

2.6. Animal model

Specific pathogen free (SPF) grade BALB/c female mice were purchased from Shanghai SLAC Laboratory Animal Co., Ltd. and used under protocols approved by the Laboratory Animal Center of Soochow University. The tumors used to investigate their evolution were grafted by subcutaneous inoculation of 2×10^6 4T1 cells (in about 50 μL PBS) into the right flank region on the back of each mouse. The orthotopic breast tumor was similarly grafted into the right side of the third-pair mammary gland of the mouse.

2.7. Blood circulation behavior of core-shell NaYF₄:5%Nd@NaGdF₄ NCs

Five healthy BALB/c mice were intravenously injected with the core-shell NCs at a dosage of 20 mg/kg. Blood samples were drawn from their eye sockets at different time points of post injection, i.e., 3 min, 10 min, 30 min, 1 h, 2 h, 4 h, 8 h, 12 h, 24 h and 48 h. The contents of Gd in the blood samples were measured by inductively coupled plasma–mass spectroscopy (ICP-MS) after they were digested with a mixture of HNO₃ and H₂O₂ (HNO₃/H₂O₂ = 2:1 by volume). The decay curve of Gd contents in the blood was fitted with an exponent quadratic model.

2.8. NIR II fluorescence imaging

In-vivo NIR II fluorescence imaging was performed with a NIR II Imaging System (Serious II 900–1700) manufactured by Suzhou NIR-Optics Co., Ltd. (China). The power density of 808-nm laser was set to 45 mW/cm², and all NIR II images were collected with an exposure time of 150 ms. The mice were anaesthetized by intraperitoneal injection of 1% pentobarbitalum aqueous solution (125 μL). After pre-contrast images were collected, the anaesthetized mice were intravenously injected with a physiological saline solution of DSPE-PEG₂₀₀₀ modified NaYF₄:5%Nd@NaGdF₄ NCs (8 mg/mL, 150 μL), followed by the acquisition of NIR II photoluminescence images at different time points.

2.9. MRI imaging

In-vitro MRI imaging was performed with a 0.5 T MRI scanner (NM120-015V-I). The longitudinal relaxivity (i.e., r_1) of NaYF₄:5%Nd@NaGdF₄ NCs was measured from a series of solutions with different concentrations of Gd³⁺ (0.4, 0.8, 1.6, 3.2, 6.4 mM). The *in-vitro* T₁-weighted MRI images were also collected. The *in-vivo* MRI imaging was performed on a 1 T MRI scanner (NM42-040H-I) after the mice were anesthetized with isoflurane. The *in-vitro* and *in-vivo* imaging instruments were provided by Suzhou Niumag Analytical Instrument Corporation.

2.10. CT imaging

The performance of modified core-shell NCs as a contrast agent for CT imaging was compared with that of core nanoparticles. They were dissolved in aqueous solutions with concentrations of 0, 0.94, 1.88, 3.75, 7.5, 15 mM, respectively. For *in-vivo* CT imaging, the tumor-bearing mice were anesthetized with isoflurane, and then intravenously injected with 200 μL core-shell NaYF₄:5%Nd@NaGdF₄ NC saline solution (12 mg/mL). The mice were anesthetized with isoflurane throughout the imaging process. The images were scanned in an accurate mode using full angle, 3 frame averaging, a 615 mA tube current, and 55 kV tube voltage.

2.11. Histological analysis

To assess the histology of tumor tissues from different growth time (*i.e.*, 1 day, 4 days, 8 days and 12 days), all tumors were harvested after the completion of NIR II imaging, and then fixed in 10% neutral buffered formalin, processed routinely into paraffin, sectioned into thin slices, and stained with H&E for histological analysis. To assess the influence of administrated core-shell NCs on the healthy mice, their major organs (heart, liver, spleen, lung, kidney) were harvested on day 10 after the mice were intravenously injected with core shell NCs, and then treated with the same procedure for histological analysis.

2.12. Hemanalysis

Four groups of healthy BALB/c mice were intravenously injected with NaYF₄:5%Nd@NaGdF₄-DSPE-PEG₂₀₀₀ NCs with a dose of 20 mg/kg, and then sacrificed on day 1, day 7, day 10 and day 15 respectively, to collect blood samples for analysis. All blood samples were tested to obtain the hemanalysis data including the blood routine and blood chemistry. The results are compared with those from mice in the control group.

3. Results and discussion

3.1. Ultra-small nanocluster mediated synthesis of Nd³⁺-doped core-shell NCs

Ultra-small NaLnF₄ nanoclusters, where Ln is a lanthanide ion (*i.e.*, Ln = Y, Gd, and Nd), were prepared by the versatile LSS method [49,50] through phase transfer and separation processes at room temperature, which is contrast to hot-injection of molecular precursors or sacrificed nanoseeds in homogenous phase at high temperature [27,41–45,51]. They were employed as precursors for the core, dopant, and shell to synthesize monodisperse Nd³⁺-doped core-shell NCs with bright NIR II luminescence through a one-pot reaction (Scheme 1a).

NaYF₄ and NaGdF₄ were selected as the core- and shell materials because of their relatively low phonon energy [52] and the minimal lattice mismatch (<2%) between them (Table S1 in the Supporting Information) [44,53]. First, the purified NaYF₄ (or NaGdF₄) nanoclusters were dissolved in a high boiling-point solvent (*i.e.*, 1-octadecene, ODE) and heated to 280 °C to grow into large NaYF₄ (or NaGdF₄) core NCs. Then, NaNdF₄ nanoclusters were injected into the core solution to form Nd³⁺-doped NaYF₄ (or NaGdF₄) NCs. After that, NaGdF₄ (or NaYF₄) nanoclusters were injected into the reaction mixture to form the uniform core-shell NCs. In contrast to the well-known nucleation-growth mechanism of NCs prepared by hot-injection of molecular precursors, the use of nanoclusters can avoid the burst of nucleation and the influence of by-products generated from decomposition of molecular precursor, and can result in core-shell NCs with a narrow size distribution [54–56].

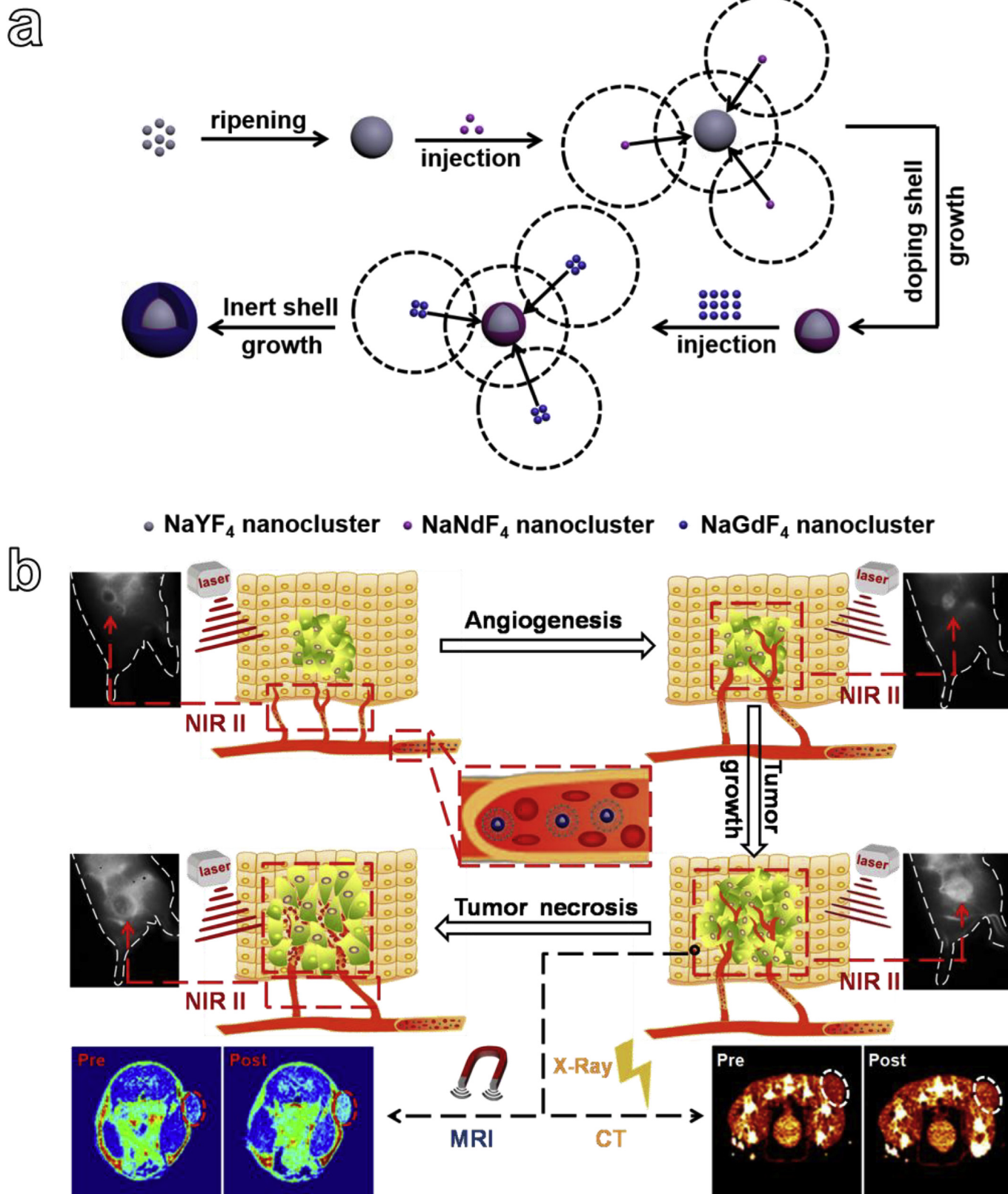
3.2. Characterization of Nd³⁺-doped NCs

The obtained core-shell NCs were characterized by various facilities to reveal their size, morphology, structure, components, and properties. TEM images of core NCs (NaYF₄:5%Nd), shell precursor (NaGdF₄ nanoclusters), and core-shell NaYF₄:5%Nd@NaGdF₄ NCs are shown in Fig. 1a–c. For comparison, the TEM image of a mixture of NaYF₄:5%Nd core NCs and shell precursor is also presented in Fig. S1a. The corresponding size distributions of core, shell and core-shell nanoparticles in Fig. S1b demonstrate an obvious change of particle size after growth of NaGdF₄ shell. The favorable growth of ultra-small NaGdF₄ nanoclusters [(2.0 ± 0.4) nm] on the surface

of larger cores [45,54,55] led to around 9 nm increments in the size of final core-shell NCs (Figs. S2a and b). High-angle annular dark field – scanning TEM (HAADF-STEM) and high-resolution STEM images of NaYF₄:5%Nd@NaGdF₄ NCs (Fig. 1d and e) clearly show the core-shell nanostructure with distinct contrast between the core and shell. The elemental mappings (Fig. 1f and g) and the line scan spectra from energy-dispersive X-ray spectroscopy (EDS) of a single core-shell NC (Fig. 1h) confirm the Y-based core and Gd-based shell, respectively. The lattice spacings for the core and shell shown in a typical high-resolution TEM image (Fig. 1i) are ~2.91 Å and ~5.16 Å, respectively, matching well with the (101) planes of NaYF₄ and the (100) planes of NaGdF₄. The sharp and resolved X-ray diffraction (XRD) peaks in Fig. S4a further demonstrate the good crystallinity of core-shell NCs due to high reaction temperature.

The above characterization results demonstrate the successful preparation of monodisperse core and core-shell NCs (*i.e.*, NaYF₄:5%Nd and NaYF₄:5%Nd@NaGdF₄) through our nanocluster-mediated one-pot synthetic approach. A number of monodisperse Nd³⁺-doped downconversion NCs (*e.g.*, NaYF₄:5%Nd@NaYF₄, NaGdF₄:5%Nd, NaGdF₄:5%Nd@NaYF₄, and NaGdF₄:5%Nd@NaGdF₄) were prepared (Figs. S2c–f) by using different combinations of NaYF₄, NaGdF₄, and NaNdF₄ nanoclusters. The high-resolution TEM and HAADF-STEM image of NaGdF₄:5%Nd@NaYF₄ NCs (Fig. S3) further illustrate the successful preparation of core-shell nanostructure, in which the core size (9.1 nm) matches well with that of NaGdF₄:5%Nd NCs (9.5 ± 0.6) nm in Fig. S2d. The bright core and grey shell observed in the HAADF-STEM image is attributed to the huge difference in the atomic number of Gd (Z = 64) and Y (Z = 39). The uniform size and morphology of the resultant core-shell NCs are attributed to the separation of the nucleation from the growth processes and the minimal lattice mismatch (<2%) between NaYF₄ and NaGdF₄ (Table S1). The small deviation of main peaks in their XRD patterns ($\Delta 2\theta < 3^\circ$, Figs. S4a and b) further illustrates the small lattice mismatch between the core and the shell.

All the resultant Nd³⁺-doped core-shell NCs exhibit bright photoluminescence, especially the core-shell NCs. Four types of Nd³⁺-doped core-shell NCs (*i.e.*, NaYF₄:5%Nd@NaYF₄, NaYF₄:5%Nd@NaGdF₄, NaGdF₄:5%Nd@NaGdF₄, and NaGdF₄:5%Nd@NaYF₄) were selected to investigate their optical properties. They exhibit similar UV–Vis–NIR absorbance due to their similar structure and compositions, although their photoluminescence intensity in the NIR II window is quite different. To quantify their relative photoluminescence quantum yields (QYs), inductively coupled plasma – atomic emission spectrometry (ICP-AES) was used to determine concentrations of Gd³⁺ and Y³⁺ ions. The molar concentration of these core-shell NCs was set at 0.1 mol/L to allow comparison of their downconversion luminescence under 808 nm excitation. Their photoluminescence spectra in Fig. S4c clearly show that the NaYF₄:5%Nd@NaGdF₄ NCs possess the strongest luminescence. To further verify it, their relative photoluminescence QYs were quantified by using the standard NIR dye IR-26 as a reference, which has a QY of 0.5% under 785 nm excitation [57]. The UV–Vis–NIR absorbance spectra of these core-shell NCs in cyclohexane and their photoluminescence spectra, together with that of IR-26 in dichloroethane under 785 nm excitation, are shown in Figs. S4d–f. The absorbance of IR-26 at 785 nm (A_s) and the integral area of its fluorescence under excitation at 785 nm (F_s) were characterized as 0.061 and 5.75×10^{-10} . The absorbance of these core-shell NCs at 785 nm (A_u) and the integral areas of their fluorescence under excitation at 785 nm (F_u) are listed in Table S2. Although 785 nm is not the optimal excitation wavelength for Nd³⁺-doped NCs [37,38] and the integral area only covers the emission in the NIR II region, it is sufficient to verify which type of NCs possess the strongest luminescence. Their relative QYs were calculated by the equation $[QY_u = QY_s \cdot (F_u/F_s) \cdot (A_s/A_u) \cdot (G_u/G_s)^2]$, in which G_u and G_s



Scheme 1. (a) Schematic illustration of the synthesis of NaYF₄:5%Nd@NaGdF₄ core-shell NCs, (b) their application in NIR II, MRI, and CT imaging of tumor from tumorigenesis, growth and necrosis.

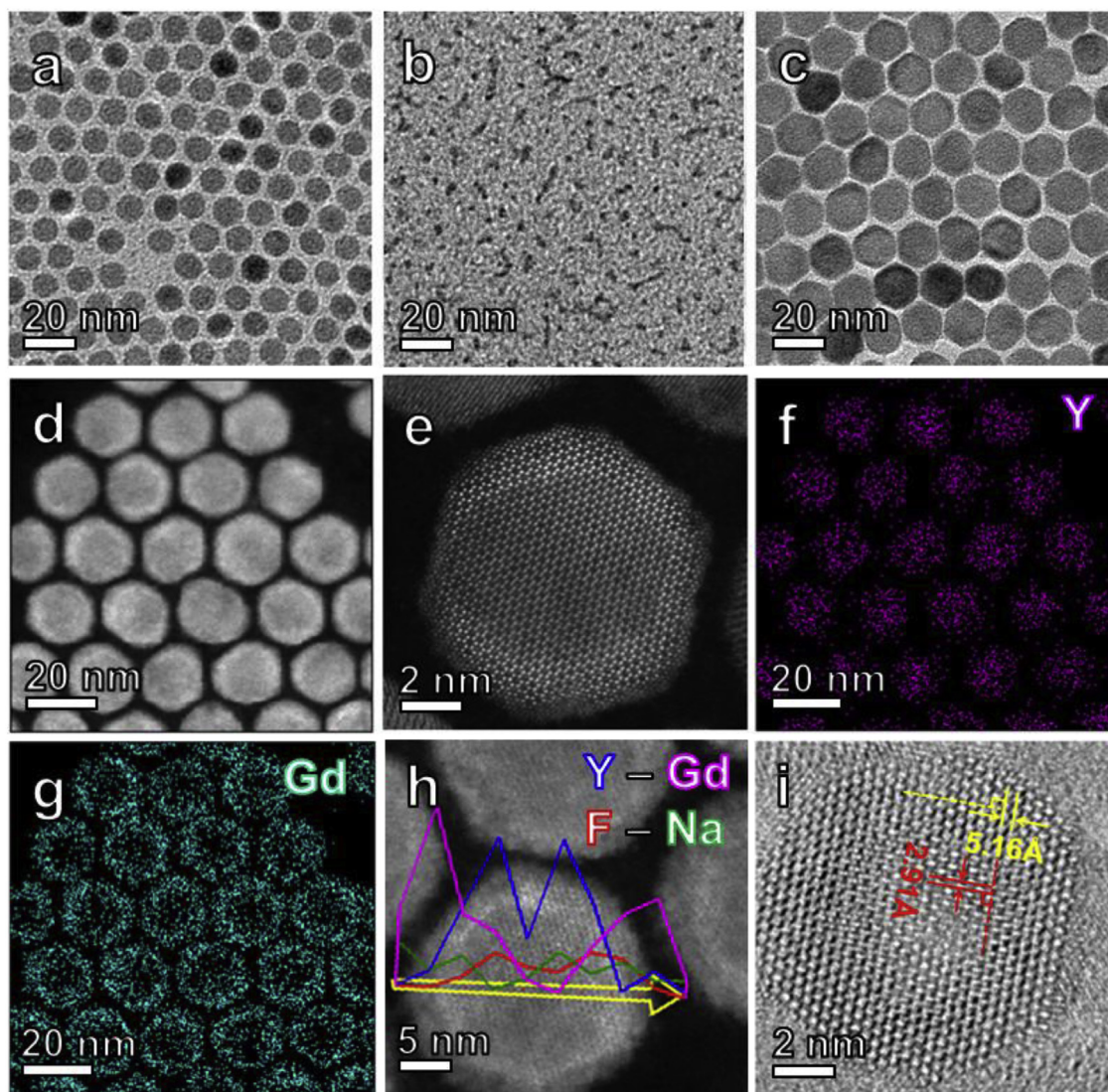


Fig. 1. TEM images of (a) NaYF₄:5%Nd core NCs, (b) NaGdF₄ nanoclusters for growth of shell, and (c) core-shell NaYF₄:5%Nd@NaGdF₄ NCs; (d) HAADF-STEM image, (e) high-resolution STEM image, (f, g) element mappings corresponding to (d), (h) magnification of (d) with EDS line scans, and (i) high-resolution TEM image of NaYF₄:5%Nd@NaGdF₄ NCs.

are the refractive indices of the solvents for the NCs and the IR-26. The results in Table S2 show that NaYF₄:5%Nd@NaGdF₄ NCs have a relative QY of 0.52%, which is the highest among core-shell NCs and comparable to that of the standard dye IR-26. The bright luminescence could be attributed to the core-shell structure. For the same type of core-shell NCs prepared under the same conditions and from the same cores [58], the thicker shell could effectively reduce the surface quenching effect than the thinner shell, and lead to the stronger luminescence [46]. Although the relative QY of our NCs is lower than that of ligand-free NaGdF₄:Nd³⁺@NaGdF₄ NCs, they are bright enough for the NIR II imaging of tumor [37].

In addition to the bright NIR II luminescence, these core-shell NCs exhibit interesting magnetism [59] and attenuation towards X-rays [60], which make them promising not only for NIR II fluorescence imaging, but also for MRI and CT imaging. Therefore, core-shell NaYF₄:5%Nd@NaGdF₄ NCs with the highest relative QY were modified with DSPE-PEG₂₀₀₀ [61] for imaging the vasculature of tumors during their progression through multimodal imaging (Scheme 1b). The Fourier transform infrared (FTIR) spectrum of the DSPE-PEG₂₀₀₀ modified NCs (red line) is compared with those of pure DSPE-PEG₂₀₀₀ (blue curve) and oleic acid capped NaYF₄:5%

Nd@NaGdF₄ NCs (black curve) in Fig. S5a. The characteristic vibration of C-O-C bond at ~1100 cm⁻¹ from the PEG fragment of DSPE-PEG₂₀₀₀ are clearly observed in the modified core-shell NCs, which demonstrates the successful surface modification through the hydrophobic-hydrophobic interactions between oleic acid and DSPE-PEG₂₀₀₀.

The hydrodynamic size of modified NaYF₄:5%Nd@NaGdF₄ NCs in the saline solution (0.9 wt% NaCl) was determined to be 48.6 nm by the dynamic light scattering (DLS) method (Fig. 2a), and was fluctuated around 50 nm over a week, which suggests their excellent colloidal stability after modification with DSPE-PEG₂₀₀₀ (Fig. S5b). Their fluorescence intensity at 1060 nm was decreased by nearly 2.9 times after surface modification (Fig. S5c), but it is 16 times stronger than hydrophilic NaYF₄:5%Nd core NCs at the same molar concentration (Fig. 2b). Their CT value is also 3.5 times stronger than modified core NCs (Fig. 2c). These results demonstrate the significance of growing NaGdF₄ shells on core NCs. The shell not only effectively reduced the surface defects to enhance downconversion luminescence, but also improved X-ray attenuation capability due to the higher atomic number of gadolinium (Z = 64) than that of yttrium (Z = 39).

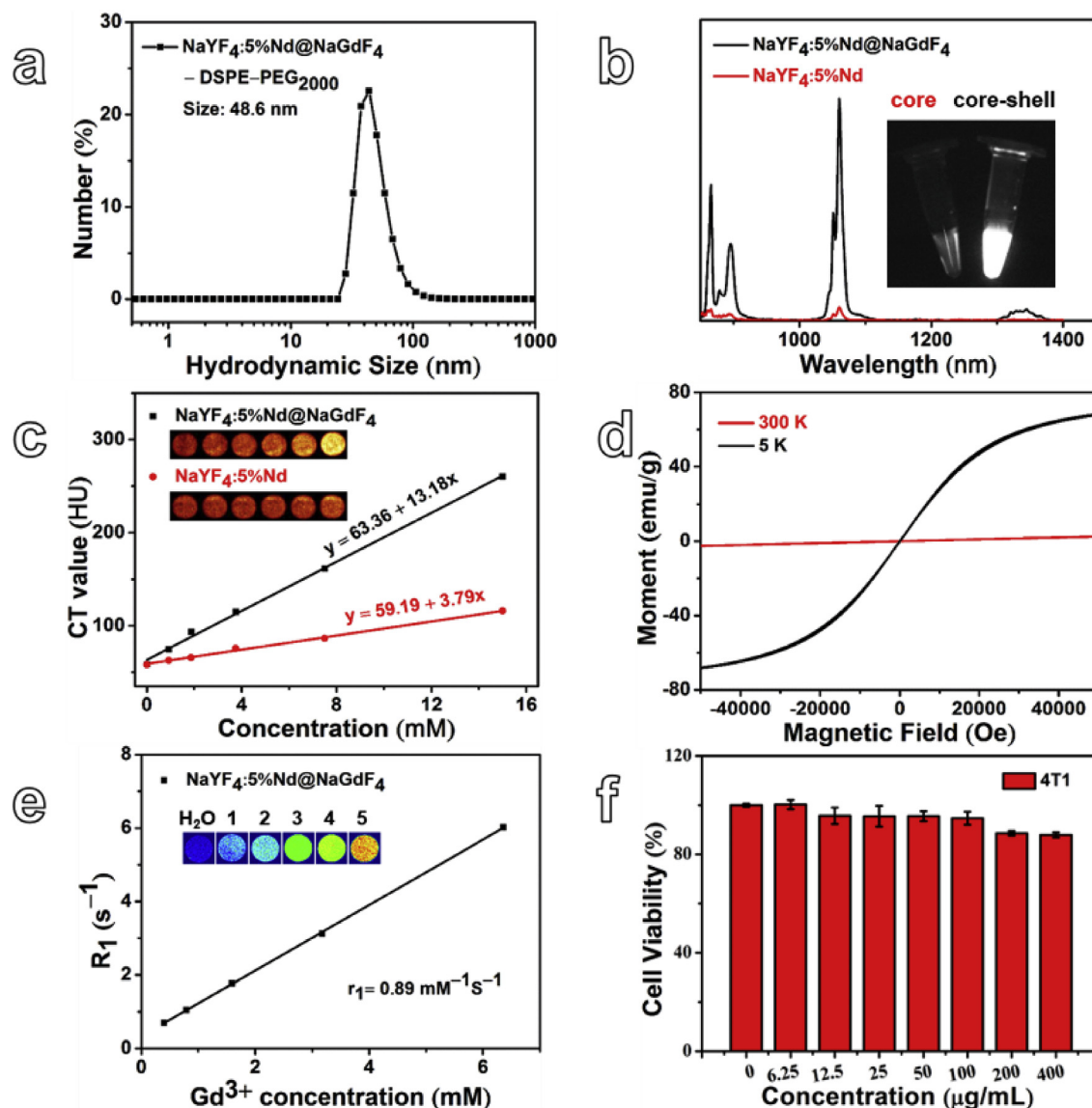


Fig. 2. (a) Hydrodynamic size of NaYF₄:5%Nd@NaGdF₄-DSPE-PEG₂₀₀₀ NCs dispersed in saline solution (0.9 wt% NaCl); (b) comparison of *in-vitro* downconversion luminescence spectra under 808 nm excitation between DSPE-PEG₂₀₀₀ decorated core (NaYF₄:5%Nd) and core-shell (NaYF₄:5%Nd@NaGdF₄) NCs (inset: photograph of solutions under 808 nm excitation); and (c) *in-vitro* CT values of DSPE-PEG₂₀₀₀ decorated core and core-shell NCs dispersed in physiological saline with same molar concentration gradient (0, 0.94, 1.88, 3.75, 7.5, 15 mM), with the inset showing photographs of CT images obtained from different concentrations; (d) magnetization isotherms of oleic acid coated NaYF₄:5%Nd@NaGdF₄ NCs at 5 K and 300 K; (e) *in-vitro* longitudinal proton relaxation of NaYF₄:5%Nd@NaGdF₄-DSPE-PEG₂₀₀₀ NCs with different concentrations of Gd³⁺ (0.4, 0.8, 1.6, 3.2, 6.4) mM, with the inset showing T₁-weighted MRI images with different concentrations; (f) relative cell viabilities of 4T1 cells after incubation with NaYF₄:5%Nd@NaGdF₄-DSPE-PEG₂₀₀₀ NCs for 24 h.

The core-shell NaYF₄:5%Nd@NaGdF₄ NCs also exhibit paramagnetism with a small value of 2.48 emu/g at 300 K and a larger value of 67.92 emu/g at 5 K (Fig. 2d). The dependence of proton relaxation on the concentration of core-shell NaYF₄:5%Nd@NaGdF₄ NCs was evaluated by using a 0.5 T MRI scanner. As shown in Fig. 2e, the longitudinal relaxation is linearly increased with Gd³⁺ concentration, and the relaxivity (r_1) is calculated to be 0.89 mM⁻¹s⁻¹ at 0.5 T, which indicates their great potential in T₁-weighted MRI imaging.

3.3. Biocompatibility and safety of Nd³⁺-doped core-shell NCs

It is well known that phospholipids, as the major component of cell membrane, exhibit excellent biocompatibility [62,63]. Prior to the *in-vivo* bioimaging, the potential cytotoxicity of DSPE-PEG₂₀₀₀ modified NaYF₄:5%Nd@NaGdF₄ NCs towards 4T1 cells (murine

breast cancer cells) was evaluated by the standard MTT assay. Fig. 2f shows that the cell viabilities exceed 87%, even when the concentration of rare-earth ions (Gd³⁺ + Y³⁺) is as high as 400 µg/mL, owing to the phospholipid surface modification.

The MTT results demonstrate the *in-vitro* excellent biocompatibility of modified NaYF₄:5%Nd@NaGdF₄ NCs. To investigate their *in-vivo* biocompatibility and biosafety, four groups of healthy BALB/c mice were intravenously injected with NaYF₄:5%Nd@NaGdF₄-DSPE-PEG₂₀₀₀ NCs at a dose of 20 mg/kg, and then were sacrificed on day 1, day 7, day 10 and day 15 respectively, to collect blood samples for blood routine examination and blood biochemistry analysis, as hematological factors can reflect the inflammatory responses caused by any side effects of a foreign substance [64]. The blood indexes (Fig. 3a–f) include hemoglobin (HGB), red blood cells (RBC), white blood cells (WBC), hematocrit (HCT), platelet (PLT), and mean corpuscular volume (MCV). There is no significant

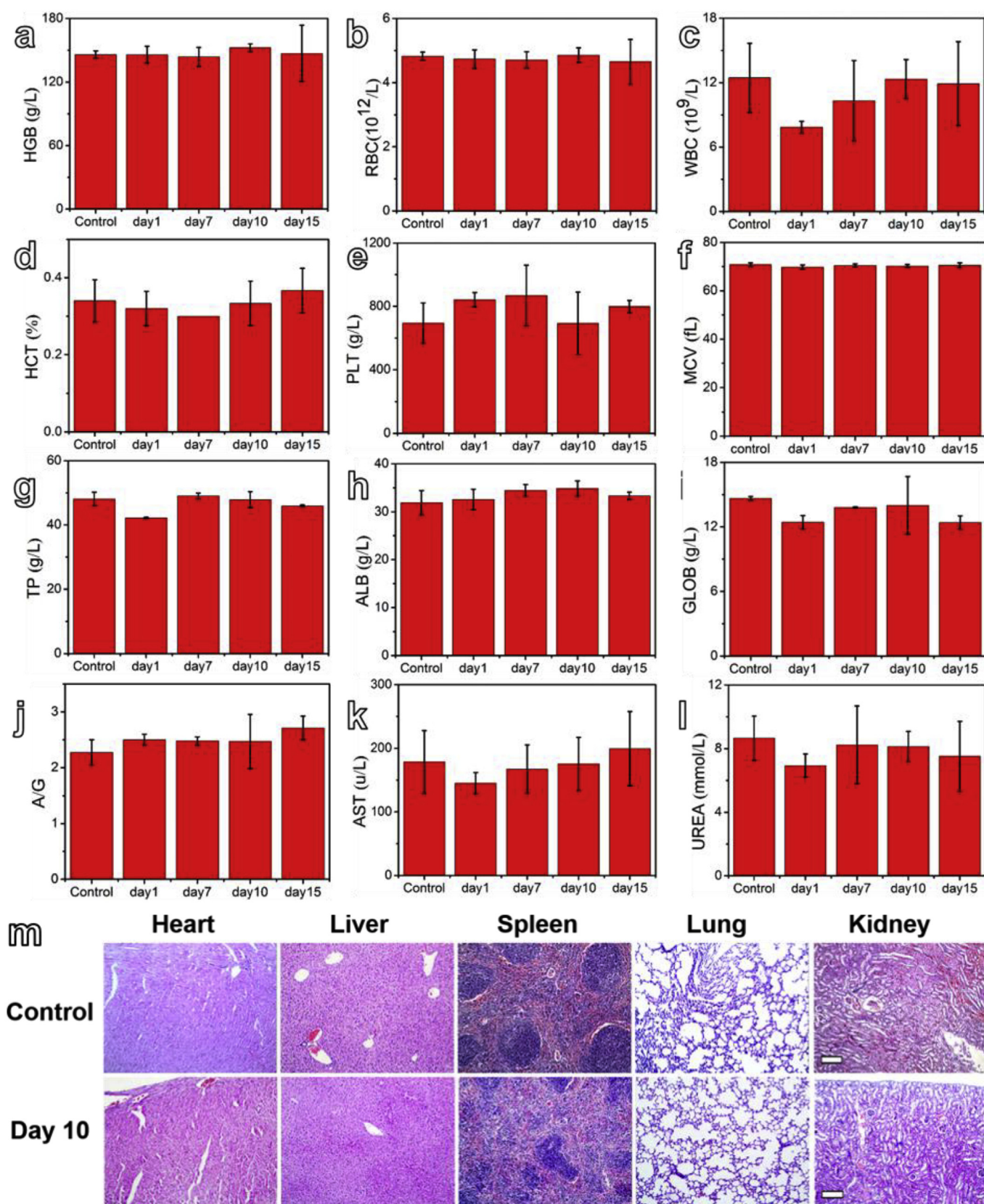


Fig. 3. Hemanalysis of BALB/c mice intravenously injected with NaYF₄:5%Nd@NaGdF₄-DSPE-PEG₂₀₀₀ NCs: blood routine test including (a) hemoglobin (HGB), (b) red blood cell count (RBC), (c) white blood cell count (WBC), (d) hematocrit (HCT), (e) platelets (PLT), (f) mean corpuscular volume (MCV); blood biochemical tests including (g) total protein (TP), (h) albumin (ALB), (i) globulin ratio of albumin (GLOB), (j) ratio of albumin to globulin (A/G), (k) aspartate aminotransferase (AST), (l) urea nitrogen (UREA). (m) H&E staining of major organs of mice from control group and experimental group on day 10, including heart, liver, spleen, lung and kidney (scale bar:100 μ m). (For interpretation of the references to color in this figure legend, the reader is referred to the Web version of this article.)

difference in RBC, HGB, MCV and HCT between the mice from the control group and experimental group. The slight decrease in WBC and slight increase in PLT in the mice from the experimental group on day 1 and day 7, and then recovery to the similar level of mice in the control group indicate a mild immunological stress.

Serum biochemical analysis (Fig. 3g–i) was carried out to show the total protein (TP), albumin (ALB), globulin ratio of albumin (GLOB), ratio of albumin to globulin (A/G), aspartate aminotransferase (AST), urea nitrogen (UREA). The slight decrease in TP and GLOB in the mice from the experimental group on day 1 suggests a disorder of immune system or a potential inflammation. Although AST and UREA, the important markers of liver function and kidney function, are slightly fluctuated, they are rather comparable with those of mice from the control group. The recovery of all indicators in the blood collected on day 10 suggests less toxicity of these core-shell NCs.

To further demonstrate the biosafety of our NCs, we further carried out hematoxylin and eosin (H&E) staining of major organs including heart, liver, spleen, lung and kidney. The images in Figs. 3m and S6 show that the structural patterns of these organs harvested on day 10 from mice in the experimental group are similar to those of mice from the control group.

The blood circulation behavior of NaYF₄:5%Nd@NaGdF₄-DSPE-PEG₂₀₀₀ NCs was assessed by determining the contents of Gd in the blood samples with ICP-MS. As shown in Fig. S7, the blood half-life time is calculated to be 5.9 h by fitting the blood circulation profile with an exponent quadratic model. The long blood half-life indicates their remarkable stability in the blood environment, and ensures their distribution in different organs and tissues for imaging.

3.4. *In-vivo* multimodal imaging of vasculature in subcutaneous breast tumor

Compared with upconversion NCs, an advantage of NaYF₄:5%Nd@NaGdF₄ NCs is their downconversion luminescence in the NIR II region, which features a higher signal-to-noise ratio and deeper penetration in comparison with visible luminescence. To demonstrate their feasibility in the NIR II imaging, a physiological saline solution of NaYF₄:5%Nd@NaGdF₄-DSPE-PEG₂₀₀₀ NCs (8 mg/mL, 150 μ L) was intravenously injected into a healthy mouse, and then NIR II photoluminescence images (Fig. S8) were acquired at different time points under excitation of an 808-nm laser. The power density of laser was 45 mW/cm², and the exposure time was 150 ms. Compared with the pre-contrast image, the liver contour and major blood vessels (labeled with red and white arrows, respectively) are clearly observed. In addition, the liver became brighter and brighter due to the gradual accumulation of NCs in liver. This control experiment demonstrates the feasibility and potential of our bright core-shell NCs in visualizing the vasculature and major organs of a mouse.

As stated previously, tumor vasculature has played significant roles in tumorigenesis, growth, necrosis, and metastasis. In order to visualize the evolution of tumor vasculature in living mice, 4T1 tumor cells (2×10^6) in phosphate buffered saline (PBS) solution were subcutaneously injected into the flank region of the right back of living BALB/c mice, which were cultured for different days to obtain different sized tumors. Then DSPE-PEG₂₀₀₀ modified NaYF₄:5%Nd@NaGdF₄ NCs (8 mg/mL, 150 μ L) were intravenously injected into tumor-bearing mice to macroscopically visualize their tumor vasculature. In contrast to imaging the tumor vasculature from the same mouse [7,11], or imaging a certain-sized tumor with well-established vasculature [9], this approach could avoid the influence of *in-vivo* retention of NCs (e.g., in the tumor and in other major organs) on tumor growth, and could obtain the clear

tendency of tumor progression through multimodal imaging.

Tumor-bearing mice were divided into four groups by the time-course of tumor growth, or by the three stages of tumor progression as illustrated in Scheme 1b (i.e. tumor angiogenesis, growth, and necrosis). Fig. 4a and Fig. S9 shows the NIR II fluorescence images of tumors grown for different days after subcutaneous inoculation of 4T1 cells. It is difficult to see mice in all pre-contrast images due to the low bio-fluorescence of mice in the NIR II window (Fig. S9). After administration of core-shell NCs, they become visible in the NIR II images due to the strong fluorescence from NCs. For the tumor grown for only 1 day (Fig. 4a, day 1), there is a dark spot (red dashed circle) in the NIR II fluorescence images acquired at 1 min, 10 min, 20 min, and 30 min post injection of core-shell NaYF₄:5%Nd@NaGdF₄ NCs. The dark spot is the site where tumor cells were inoculated, and means the absence of neo-vasculature within it. The fluorescence from the periphery of dark spot was clearly observed 1 min after injection, and the contrast was gradually enhanced with the circulation of NCs. More importantly, the neo-vasculature (pointed by white arrows) connected with the dark spot is clearly observed.

The photograph in Fig. 5a₁ also shows that in comparison with healthy mouse in Fig. S10a, a tiny lump with a volume of 36.6 mm³ (calculated from the equation $V = ab^2/2$, $a = 5.09$ mm, $b = 3.79$ mm) was developed within 24 h after the injection of tumor cells. The intense hyperemia at the injection site [65] could explain the notable contrast between the lump and its periphery in the NIR II images. To further understand this phenomenon, the hematoxylin and eosin (H&E) staining of longitudinal section of epidermal tissue from healthy mouse (Figs. S10b–d) and the lump (Fig. 5b) were performed. A slight increment in the abundance of blood vessels in derma is observed. Moreover, an obvious dilatation of capillaries (labeled with red arrows in Fig. 5b), which is consistent with the macroscopic hyperemia phenomenon around inoculation area, demonstrate the proliferation of tumor cells (black dashed area in Fig. 5b₁) [65]. Although highly concentrated Nd³⁺-doped NCs could produce heat upon irradiation with the high-power-density laser [66], the heating effect of our Nd³⁺-doped NCs on the normal skin and tumor tissue is negligible due to the low dopant concentration and low power density of laser (45 mW/cm²) during the imaging process.

On day 4 after inoculation of tumor cells, the hyperemia at the inoculation site has disappeared, and the tumor (Fig. 5a₂) remains the similar size ($V = 34.7$ mm³, $a = 4.64$ mm, $b = 3.87$ mm) in comparison with that developed after inoculation for 1 day (Fig. 5a₁, 36.6 mm³). After intravenous injection of core-shell NaYF₄:5%Nd@NaGdF₄ NCs, the major vessels (pointed by white arrows) around the tumor are clearly observed 1 min post injection (Fig. 4a, day 4). With the circulation of NCs and their infiltration into tumor (red dashed circle), the tumor gradually became bright, and the tumor-to-background ratio is steadily enhanced within 20 min post injection (Fig. 4b). The tumor-to-background ratio is calculated by the ratio between the average signal of tumor and the average noise of background [7]. Although this ratio calculated from the results obtained at 30 min is only 0.58 lower than that obtained at 20 min, the contrast between the tumor and its periphery is much clearer due to the decrease of NCs from the surrounding vessels. Unlike the absence of vasculature in the tumor grown for 1 day, the above imaging results illustrate the formation of neo-vasculature within tumor at this stage. In addition, the observed surrounding vessels are also more than those observed in tumor grown for 1 day.

To further confirm the formation of neo-vasculature within tumor, the tumor was dissected and sliced in the longitudinal direction for H&E staining. The images in Fig. 5c clearly shows that the derma has become much thinner, accompanied by a decrease in the vessels in comparison with those in Fig. 5b, mainly due to the

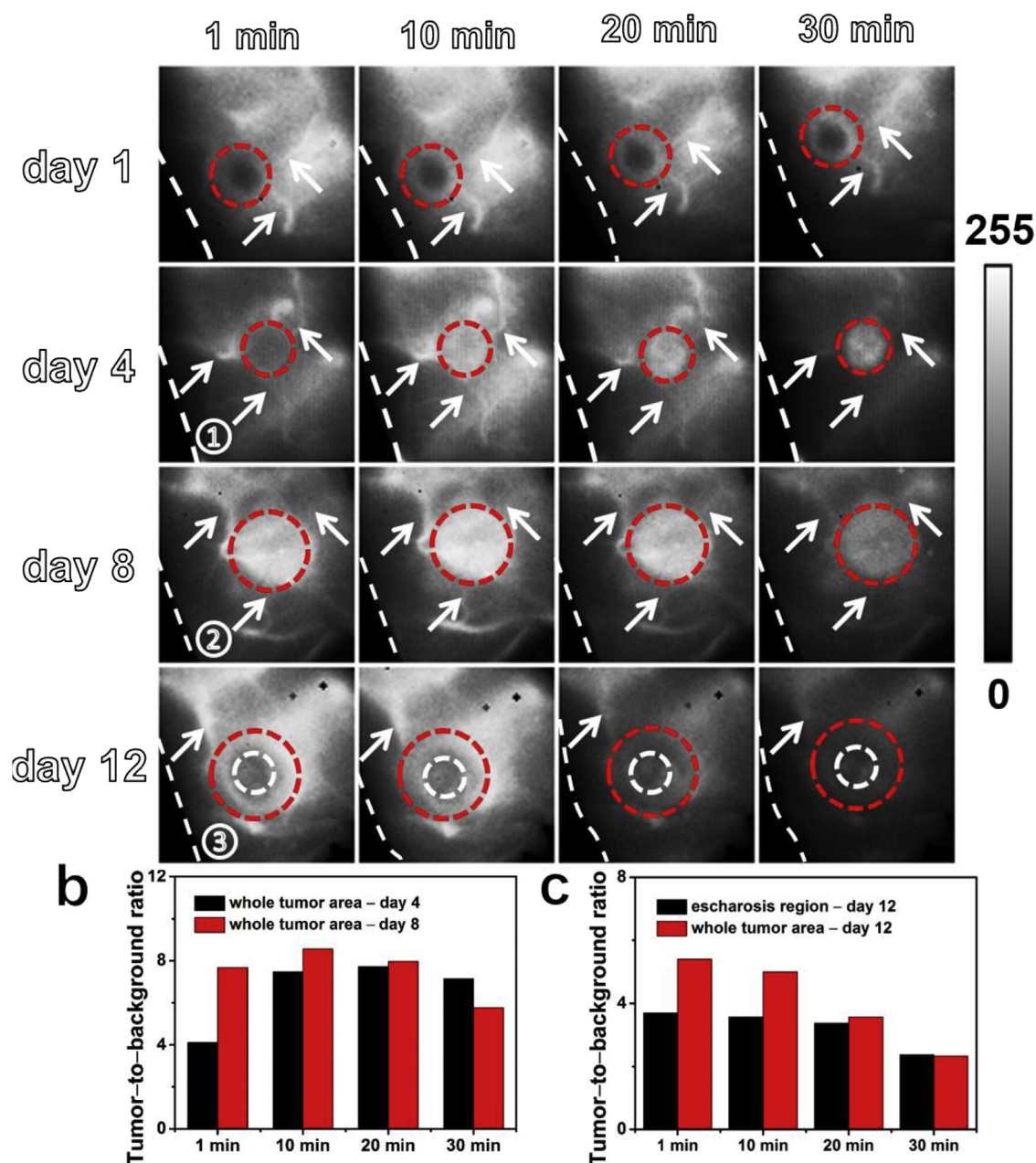


Fig. 4. (a) *In-vivo* NIR II images of tumors (red dashed cycles) grown for different days after subcutaneous inoculation of 4T1 tumor cells; time-course of tumor growth covers three stages of tumor angiogenesis, growth, and necrosis; the NIR II images clearly shows the formation and variation of tumor vasculature (pointed by white arrows). (b–c) Time-dependent tumor-to-background ratios determined by the average signal of tumor (red dashed cycles) and the average noise of background (white solid cycles) shown in (a). (For interpretation of the references to color in this figure legend, the reader is referred to the Web version of this article.)

invasion of tumor cells. In addition, many different sized vessels are found in loose tumor tissue (Fig. 5c₁), which are responsible for the infiltration and retention of NCs in tumor.

When the tumor has grown for 8 days to achieve a size around 5 fold larger (Fig. 5a₃, $V = 166.7 \text{ mm}^3$, $a = 7.94 \text{ mm}$, $b = 6.48 \text{ mm}$) than that grown for 4 days. NIR II images were collected at the same time intervals after intravenous injection of core-shell NC solution (Fig. 4a, day 8). In contrast to the results of NIR II imaging of tumor grown for 4 days, the fluorescence from the whole tumor area (red dashed circle) is rapidly enhanced after intravenous injection of NCs, and the tumor-to-background ratio is nearly 1.9 fold higher than that from the tumor grown for 4 days (Fig. 4b). Since there is no obvious increase in neo-vasculature around the tumor area

(white arrow pointed), the stronger signal is attributed to the abundant well-established vasculature within the tumor. This result is supported by the H&E staining of a longitudinal section of tumor in Fig. 5d, which reveals an abundance of capillaries and increasing compactness of tumor compared with that excised on day 4.

After the tumor grew for 12 days, the tumor was necrotized to form escharosis (Fig. 5a₄), due to the insufficient supply of nutrients and oxygen during the proliferation of tumor cells, and the same NIR II imaging procedure was performed to reveal the signal enhancement around the tumor (Fig. 4a, day 12). The whole tumor area and its escharosis region are labeled with red- and white dashed circles respectively, and their tumor-to-background ratios

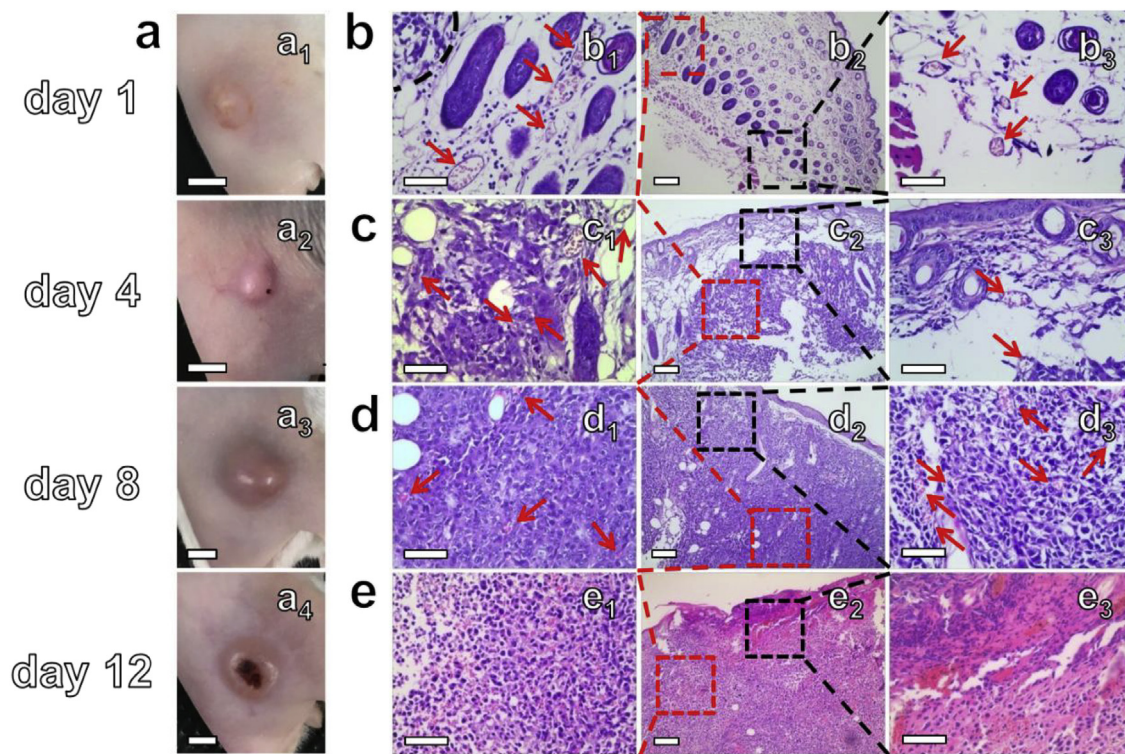


Fig. 5. (a) Photographs of mice bearing tumors grown for different days after subcutaneous inoculation of 4T1 tumor cells after different numbers of days, and used for the NIR II imaging (scale bar: 5 mm), (b–e) H&E staining of corresponding tumor longitudinal sections from tumor-bearing mice shown in Fig. 5a (scale bar: 100 μ m).

are shown in Fig. 4c. Although the major vessels (pointed by white arrow) are still visible, the continuous decline of their tumor-to-background ratios indicate the difficult circulation and retention of NCs within tumor, which is very likely due to the angioneclerosis in the tumor and the formation of escharosis.

The angioneclerosis in the tumor is confirmed by the results from H&E staining of tumor longitudinal sections (Fig. 5e). Massive erythrocytes are effused from broken vessels, and diffused with inflammatory cells and necrotic cells, as shown in Fig. 5e₁ and Fig. 5e₃. The angioneclerosis in the tumor and the formation of escharosis suggest the possible occurrence of tumor metastasis at this stage, as earlier studies have revealed that subcutaneous 4T1-tumor-bearing mice with serious escharosis had obvious tumor metastasis to major organs like lung and liver [60,67].

Although the NIR II imaging features noninvasive real-time feedback with high sensitivity [12,18], it has limited penetration in comparison with MRI and CT imaging. As demonstrated in Fig. 2, core-shell NaYF₄:5%Nd@NaGdF₄ NCs have great potential in MRI and CT imaging due to their room-temperature paramagnetism and their capability of attenuating X-rays. Since the tumor grown for 8 days (with a size of 166.7 mm³) has well-established vasculature, MRI and CT imaging were performed on mice bearing such tumors to provide complementary information. Fig. 6a displays the color-mapped MRI images collected at 20 min, 40 min, and 60 min on a 1 T MRI scanner, after intravenous injection of NC saline solution (5 mg/mL, 200 μ L) into a tumor-bearing mouse. Compared with the pre-contrast image, obvious enhancement is observed in the tumor longitudinal section (red dashed circle), which is consistent with the NIR II imaging results. The *in-vivo* CT images (Fig. 6b) further confirm the enhancement in the tumor (white dashed circle) after intravenous injection of 200 μ L saline solution of core-shell NaYF₄:5%Nd@NaGdF₄ NCs (12 mg/mL). The CT values are

increased from 25.86 HU for the pre-contrast image to 46.80 HU for image acquired at 30 min post-injection of NCs (Fig. 6c). The results obtained from the NIR II fluorescence imaging, MRI, and CT imaging demonstrate the potential of core-shell NaYF₄:5%Nd@NaGdF₄ NCs for multimodal imaging of tumor and its vasculature, which is responsible for the circulation and accumulation of NCs in tumor tissue.

3.5. *In-vivo* NIR II imaging of vasculature in orthotopic breast tumor

Since the vasculature of a tumor implanted in the flank region of mouse could be different from that of an orthotopic tumor, an orthotopic breast tumor was implanted on the right side of the third-pair mammary gland of a mouse for visualization of its vasculature through NIR II fluorescence imaging with our core-shell NaYF₄:5%Nd@NaGdF₄ NCs. The NIR II images of a healthy mouse (Fig. 6d₁) and an orthotopic tumor-bearing mouse (Fig. 6d₂) were collected after intravenous injection of NC solution (8 mg/mL, 200 μ L). In comparison with the tumor implanted in flank region (Fig. 4a), the vessels across tumor surface and those around the tumor contour are observed with low contrast, although the corresponding H&E staining of its longitudinal section (Fig. 6e₁) reveals abundant blood vessels in the tumor. The observed discrepancy could be attributed to differences in the tumor location [6]. In addition, a bright spot (indicated by red arrows in Fig. 6d) is clearly observed in the right inguinal region in both mice, which is confirmed to be a vascular intersection after dissection of them (Fig. 6e₃, red arrow). These results further demonstrate the potential of core-shell NaYF₄:5%Nd@NaGdF₄ NCs in NIR II imaging of vasculature.

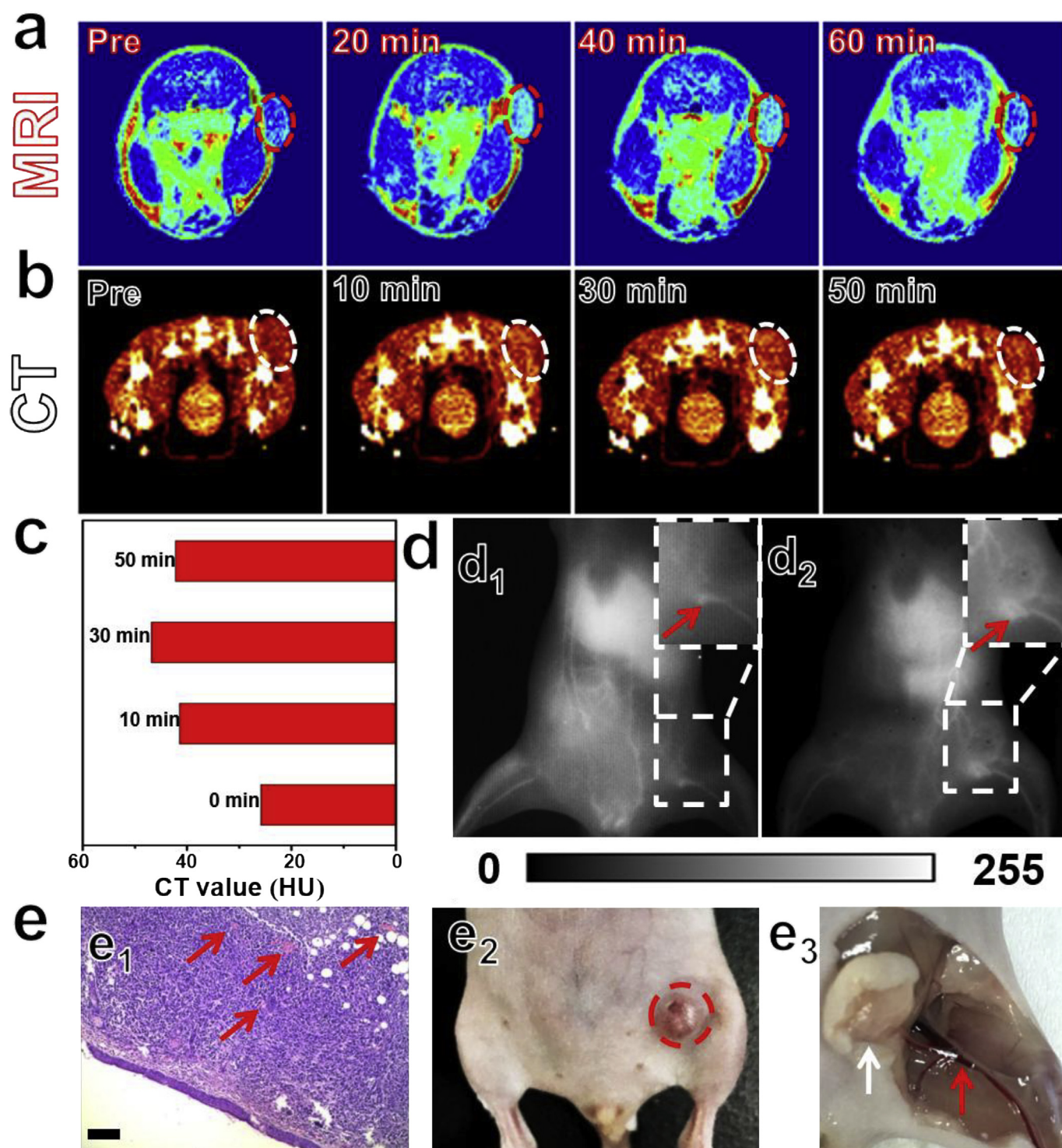


Fig. 6. (a–b) *In-vivo* T_1 -weighted MRI images and CT images of mice bearing 4T1 tumors, collected before and after intravenous injection of 200 μ L NaYF₄:5%Nd@NaGdF₄-DSPE-PEG₂₀₀₀ NCs physiological saline solution at different time points, the nanoagent concentrations for MRI and CT imaging are 5 mg/mL and 12 mg/mL, respectively; (c) corresponding CT signal intensity of tumor sections; (d) *in-vivo* NIR II images of a healthy mouse (d₁) and an orthotopic tumor-bearing mouse (d₂) after intravenous injection of NaYF₄:5%Nd@NaGdF₄-DSPE-PEG₂₀₀₀ NCs in physiological saline solution (8 mg/mL, 200 μ L); (e₁) H&E staining of tumor longitudinal sections (scale bar:100 μ m), and corresponding photographs of orthotopic breast cancer-bearing mouse (e₂) before and after (e₃) dissection. The red and white arrows point to the vascular intersection and the orthotopic tumor, respectively. (For interpretation of the references to color in this figure legend, the reader is referred to the Web version of this article.)

4. Conclusion

In summary, an ultra-small nanoclusters mediated synthetic approach was developed to prepare monodisperse Nd³⁺-doped

downconversion nanocrystals. The core-shell NaYF₄:5%Nd@NaGdF₄ NCs exhibit the strongest photoluminescence among the resultant NCs for NIR II fluorescence imaging, and possess strong paramagnetism and X-ray attenuation for MRI and CT

imaging. They were modified with DSPE-PEG_{2k} to show long blood circulation half-life (5.9 h), excellent biocompatibility and biosafety. They were successfully applied for visualization of tumor vasculature by the NIR II imaging in a breast tumor model, which was established by the subcutaneous inoculation of 4T1 cells. The formation and variation of tumor vasculature during tumorigenesis, growth and necrosis was clearly observed and further confirmed by the histological analysis. The tumor grown for 8 days after inoculation has well-established vasculature than other tumors grown for different days, demonstrated by the strongest signal obtained during the NIR II imaging, MRI imaging and CT imaging. The potential of NIR II fluorescence from our NCs in visualization of tumor vasculature was also illustrated in an orthotopic breast tumor model. These results are not only crucial for understanding of tumor progression, tumor staging, and tumor therapy, but also highlight the great potential of Nd-based rare earth nanoparticles in imaging of vasculature during tumorigenesis, thrombosis, and atherosclerosis.

Acknowledgements

Z. Li acknowledges support from the National Natural Science Foundation of China, China (81471657, 81527901), the 1000 Plan for Young Talents, China, Jiangsu Specially Appointed Professorship, China, and the Program of Jiangsu Innovative and Entrepreneurial Talents, China. The authors also are grateful for support from the Jiangsu Provincial Key Laboratory of Radiation Medicine and Protection, China, the Priority Academic Development Program of Jiangsu Higher Education Institutions (PAPD), China. The authors would like to thank Suzhou NIR-Optics Technology Co. Ltd. for providing NIR II imaging test, and also thank Dr. Tania Silver for critical reading of the manuscript.

Appendix A. Supplementary data

Supplementary data related to this article can be found at <https://doi.org/10.1016/j.biomaterials.2018.05.021>.

References

- [1] B.R. Zetter, Angiogenesis and tumor metastasis, *Annu. Rev. Med.* 49 (1998) 407–424.
- [2] J. Folkman, M. Bach, J.W. Rowe, F. Davidoff, P. Lambert, C. Hirsch, A. Goldberg, H.H. Hiatt, J. Glass, E. Henshaw, Tumor angiogenesis-therapeutic implications, *N. Engl. J. Med.* 285 (1971) 1182–1186.
- [3] N. Weidner, J.P. Semple, W.R. Welch, J. Folkman, Tumor angiogenesis and metastasis-correlation in invasive breast-carcinoma, *N. Engl. J. Med.* 324 (1991) 1–8.
- [4] U. Prabhakar, H. Maeda, R.K. Jain, E.M. Sevick-Muraca, W. Zamboni, O.C. Farokhzad, S.T. Barry, A. Gabizon, P. Grodzinski, D.C. Blakey, Challenges and key considerations of the enhanced permeability and retention effect for nanomedicine drug delivery in oncology, *Canc. Res.* 73 (2013) 2412–2417.
- [5] J.A. Barreto, W. O'Malley, M. Kubeil, B. Graham, H. Stephan, L. Spiccia, Nanomaterials: applications in cancer imaging and therapy, *Adv. Mater.* 23 (2011) 18–40.
- [6] J.L. Perry, K.G. Reuter, J.C. Luft, C.V. Pecot, W. Zamboni, J.M. DeSimone, Mediating passive tumor accumulation through particle size, tumor type, and location, *Nano Lett.* 17 (2017) 2879–2886.
- [7] C.H. Song, Y.J. Zhang, C.Y. Li, G.C. Chen, X.F. Kang, Q.B. Wang, Enhanced nanodrug delivery to solid tumors based on a tumor vasculature-targeted strategy, *Adv. Funct. Mater.* 26 (2016) 4192–4200.
- [8] W. Gao, S. Li, Z. Liu, Y. Sun, W. Cao, L. Tong, G. Cui, B. Tang, Targeting and destroying tumor vasculature with a near-infrared laser-activated “nanobomb” for efficient tumor ablation, *Biomaterials* 139 (2017) 1–11.
- [9] J. Liu, P. Wang, X. Zhang, L. Wang, Z. Wang, Z. Gu, J. Tang, M. Guo, M. Cao, H. Zhou, Y. Liu, C. Chen, Rapid degradation and high renal clearance of Cu₃BiS₃ nanodots for efficient cancer diagnosis and photothermal therapy in vivo, *ACS Nano* 10 (2016) 4587–4598.
- [10] Z.J. Zhou, C.Q. Wu, H.Y. Liu, X.L. Zhu, Z.H. Zhao, L.R. Wang, Y. Xu, H. Ai, J.H. Gao, Surface and interfacial engineering of iron oxide nanoplates for highly efficient magnetic resonance angiography, *ACS Nano* 9 (2015) 3012–3022.
- [11] C. Li, Y. Zhang, M. Wang, Y. Zhang, G. Chen, L. Li, D. Wu, Q. Wang, In vivo real-time visualization of tissue blood flow and angiogenesis using Ag₂S quantum dots in the NIR-II window, *Biomaterials* 35 (2014) 393–400.
- [12] G. Hong, J.C. Lee, J.T. Robinson, U. Raaz, L. Xie, N.F. Huang, J.P. Cooke, H. Dai, Multifunctional in vivo vascular imaging using near-infrared II fluorescence, *Nat. Med.* 18 (2012) 1841–1846.
- [13] A.M. Smith, M.C. Mancini, S. Nie, Bioimaging: second window for in vivo imaging, *Nat. Nanotechnol.* 4 (2009) 710–711.
- [14] Y. Tsukasaki, A. Komatsuzaki, Y. Mori, Q. Ma, Y. Yoshioka, T. Jin, A short-wavelength infrared emitting multimodal probe for non-invasive visualization of phagocyte cell migration in living mice, *Chem. Commun.* 50 (2014) 14356–14359.
- [15] S. Diao, J.L. Blackburn, G. Hong, A.L. Antaris, J. Chang, J.Z. Wu, B. Zhang, K. Cheng, C.J. Kuo, H. Dai, Fluorescence imaging in vivo at wavelengths beyond 1500 nm, *Angew. Chem. Int. Ed.* 54 (2015) 14758–14762.
- [16] S. Diao, G. Hong, J.T. Robinson, L. Jiao, A.L. Antaris, J.Z. Wu, C.L. Choi, H. Dai, Chirality enriched (12,1) and (11,3) single-walled carbon nanotubes for biological imaging, *J. Am. Chem. Soc.* 134 (2012) 16971–16974.
- [17] D. Franke, D.K. Harris, O. Chen, O.T. Bruns, J.A. Carr, M.W. Wilson, M.G. Bawendi, Continuous injection synthesis of indium arsenide quantum dots emissive in the short-wavelength infrared, *Nat. Commun.* 7 (2016) 12749.
- [18] G. Hong, J.T. Robinson, Y. Zhang, S. Diao, A.L. Antaris, Q. Wang, H. Dai, In vivo fluorescence imaging with Ag₂S quantum dots in the second near-infrared region, *Angew. Chem. Int. Ed.* 51 (2012) 9818–9821.
- [19] C. Li, Y. Zhang, G. Chen, F. Hu, K. Zhao, Q. Wang, Engineered multifunctional nanomedicine for simultaneous stereotactic chemotherapy and inhibited osteolysis in an orthotopic model of bone metastasis, *Adv. Mater.* 29 (2017), 1605754.
- [20] A.L. Antaris, H. Chen, K. Cheng, Y. Sun, G.S. Hong, C.R. Qu, S. Diao, Z.X. Deng, X.M. Hu, B. Zhang, X.D. Zhang, O.K. Yaghi, Z.R. Alamparambil, X.C. Hong, Z. Cheng, H.J. Dai, A small-molecule dye for NIR-II imaging, *Nat. Mater.* 15 (2016) 235–242.
- [21] K.Q. Shou, C.R. Qu, Y. Sun, H. Chen, S. Chen, L. Zhang, H.B. Xu, X.C. Hong, A.X. Yu, Z. Cheng, Multifunctional biomedical imaging in physiological and pathological conditions using a NIR-II probe, *Adv. Funct. Mater.* 27 (2017), 1700995.
- [22] X.D. Zhang, H.S. Wang, A.L. Antaris, L.L. Li, S. Diao, R. Ma, A. Nguyen, G.S. Hong, Z.R. Ma, J. Wang, S.J. Zhu, J.M. Castellano, T. Wyss-Coray, Y.Y. Liang, J. Luo, H.J. Dai, Traumatic brain injury imaging in the second near-infrared window with a molecular fluorophore, *Adv. Mater.* 28 (2016) 6872–6879.
- [23] B. Liu, C. Li, P. Yang, Z. Hou, J. Lin, 808-nm-Light-Excited lanthanide-doped nanoparticles: rational design, luminescence control and theranostic applications, *Adv. Mater.* 29 (2017), 1605434.
- [24] R. Wang, L. Zhou, W. Wang, X. Li, F. Zhang, In vivo gastrointestinal drug-release monitoring through second near-infrared window fluorescent bioimaging with orally delivered microcarriers, *Nat. Commun.* 8 (2017) 14702.
- [25] D.J. Naczynski, M.C. Tan, M. Zevon, B. Wall, J. Kohl, A. Kulesa, S. Chen, C.M. Roth, R.E. Riman, P.V. Moghe, Rare-earth-doped biological composites as in vivo shortwave infrared reporters, *Nat. Commun.* 4 (2013) 2199.
- [26] W. Shao, G. Chen, A. Kuzmin, H.L. Kutscher, A. Pliss, T.Y. Ohulchanskyy, P.N. Prasad, Tunable narrow band emissions from dye-sensitized core/shell nanocrystals in the second near-infrared biological window, *J. Am. Chem. Soc.* 138 (2016) 16192–16195.
- [27] R. Wang, X. Li, L. Zhou, F. Zhang, Epitaxial seeded growth of rare-earth nanocrystals with efficient 800 nm near-infrared to 1525 nm short-wavelength infrared downconversion photoluminescence for in vivo bioimaging, *Angew. Chem. Int. Ed.* 53 (2014) 12086–12090.
- [28] Y. Zhong, Z. Ma, S. Zhu, J. Yue, M. Zhang, A.L. Antaris, J. Yuan, R. Cui, H. Wan, Y. Zhou, W. Wang, N.F. Huang, J. Luo, Z. Hu, H. Dai, Boosting the down-shifting luminescence of rare-earth nanocrystals for biological imaging beyond 1500 nm, *Nat. Commun.* 8 (2017) 737.
- [29] Y.F. Wang, G.Y. Liu, L.D. Sun, J.W. Xiao, J.C. Zhou, C.H. Yan, Nd³⁺-Sensitized upconversion nanophosphors: efficient in vivo bioimaging probes with minimized heating effect, *ACS Nano* 7 (2013) 7200–7206.
- [30] B. Del Rosal, D.H. Ortgies, N. Fernandez, F. Sanz-Rodriguez, D. Jaque, E.M. Rodriguez, Overcoming autofluorescence: long-lifetime infrared nanoparticles for time-gated in vivo imaging, *Adv. Mater.* 28 (2016) 10188–10193.
- [31] U. Rocha, K.U. Kumar, C. Jacinto, I. Villa, F. Sanz-Rodriguez, C. Iglesias de la Cruz Mdel, A. Juaranz, E. Carrasco, F.C. van Veggel, E. Bovero, J.G. Sole, D. Jaque, Neodymium-doped LaF₃ nanoparticles for fluorescence bioimaging in the second biological window, *Small* 10 (2014) 1141–1154.
- [32] R. Wang, F. Zhang, Near-infrared nanomaterials: preparation, bioimaging and therapy applications. Chapter 1: lanthanide-based near infrared nanomaterials for bioimaging, *RSC Nanosci. Nanotechnol.* (2016) 1–39.
- [33] X.F. Yu, L.D. Chen, M. Li, M.Y. Xie, L. Zhou, Y. Li, Q.Q. Wang, Highly efficient fluorescence of NdF₃/SiO₂ core/shell nanoparticles and the applications for in vivo NIR detection, *Adv. Mater.* 20 (2008) 4118–4123.
- [34] C. Cao, M. Xue, X. Zhu, P. Yang, W. Feng, F. Li, Energy transfer highway in Nd³⁺-Sensitized nanoparticles for efficient near-infrared bioimaging, *ACS Appl. Mater. Interfaces* 9 (2017) 18540–18548.
- [35] W. Wei, G. Chen, A. Baev, G.S. He, W. Shao, J. Damasco, P.N. Prasad, Alleviating luminescence concentration quenching in upconversion nanoparticles through organic dye sensitization, *J. Am. Chem. Soc.* 138 (2016) 15130–15133.
- [36] L. Marciniak, A. Pilch, S. Arabasz, D.Y. Jin, A. Bednarkiewicz, Heterogeneously

- Nd³⁺ doped single nanoparticles for NIR-induced heat conversion, luminescence, and thermometry, *Nanoscale* 9 (2017) 8288–8297.
- [37] G.Y. Chen, T.Y. Ohulchanskyy, S. Liu, W.C. Law, F. Wu, M.T. Swihart, H. Agren, P.N. Prasad, Core/shell NaGdF₄:Nd³⁺/NaGdF₄ nanocrystals with efficient near-infrared to near-infrared downconversion photoluminescence for bioimaging applications, *ACS Nano* 6 (2012) 2969–2977.
 - [38] Q.S. Qin, P.Z. Zhang, L.D. Sun, S. Shi, N.X. Chen, H. Dong, X.Y. Zheng, L.M. Li, C.H. Yan, Ultralow-power near-infrared excited neodymium-doped nanoparticles for long-term in vivo bioimaging, *Nanoscale* 9 (2017) 4660–4664.
 - [39] Y. Dai, D. Yang, D. Yu, C. Cao, Q. Wang, S. Xie, L. Shen, W. Feng, F. Li, Mussel-inspired polydopamine-coated lanthanide nanoparticles for NIR-II/CT dual imaging and photothermal therapy, *ACS Appl. Mater. Interfaces* 9 (2017) 26674–26683.
 - [40] Y. Liu, H. Fan, Q. Guo, A. Jiang, X. Du, J. Zhou, Ultra-small pH-responsive Nd-doped NaDyF₄ nanoagents for enhanced cancer theranostic by in situ aggregation, *Theranostics* 7 (2017) 4217–4228.
 - [41] X.M. Li, R. Wang, F. Zhang, D.Y. Zhao, Engineering homogeneous doping in single nanoparticle to enhance upconversion efficiency, *Nano Lett.* 14 (2014) 3634–3639.
 - [42] S. Fischer, J.K. Swaback, A.P. Alivisatos, Controlled isotropic and anisotropic shell growth in beta-NaLnF₄ nanocrystals induced by precursor injection rate, *J. Am. Chem. Soc.* 139 (2017) 12325–12332.
 - [43] F. Wang, R. Deng, X. Liu, Preparation of core-shell NaGdF₄ nanoparticles doped with luminescent lanthanide ions to be used as upconversion-based probes, *Nat. Protoc.* 9 (2014) 1634–1644.
 - [44] N.J. Johnson, F.C. van Veggel, Lanthanide-based heteroepitaxial core-shell nanostructures: compressive versus tensile strain asymmetry, *ACS Nano* 8 (2014) 10517–10527.
 - [45] N.J. Johnson, A. Korinek, C. Dong, F.C. van Veggel, Self-focusing by Ostwald ripening: a strategy for layer-by-layer epitaxial growth on upconverting nanocrystals, *J. Am. Chem. Soc.* 134 (2012) 11068–11071.
 - [46] S. Fischer, N.D. Bronstein, J.K. Swaback, E.M. Chan, A.P. Alivisatos, Precise tuning of surface quenching for luminescence enhancement in core-shell lanthanide-doped nanocrystals, *Nano Lett.* 16 (2016) 7241–7247.
 - [47] C. Cao, M. Xue, X. Zhu, P. Yang, W. Feng, F. Li, Energy transfer highway in Nd³⁺-sensitized nanoparticles for efficient near-infrared bioimaging, *ACS Appl. Mater. Interfaces* 9 (2017) 18540–18548.
 - [48] D.L. Ni, J.W. Zhang, W.B. Bu, H.Y. Xing, F. Han, Q.F. Xiao, Z.W. Yao, F. Chen, Q.J. He, J.N. Liu, S.J. Zhang, W.P. Fan, L.P. Zhou, W.J. Peng, J.L. Shi, Dual-targeting upconversion nanoprobe across the blood-brain barrier for magnetic resonance/fluorescence imaging of intracranial glioblastoma, *ACS Nano* 8 (2014) 1231–1242.
 - [49] J.F. Ren, G.H. Jia, Y.Y. Guo, A.X. Wang, S.Q. Xu, Unraveling morphology and phase control of NaLnF₄ upconverting nanocrystals, *J. Phys. Chem. C* 120 (2016) 1342–1351.
 - [50] X. Wang, J. Zhuang, Q. Peng, Y. Li, A general strategy for nanocrystal synthesis, *Nature* 437 (2005) 121–124.
 - [51] X. Li, D. Shen, J. Yang, C. Yao, R. Che, F. Zhang, D. Zhao, Successive layer-by-layer strategy for multi-shell epitaxial growth: shell thickness and doping position dependence in upconverting optical properties, *Chem. Mater.* 25 (2012) 106–112.
 - [52] H. Dong, L.D. Sun, C.H. Yan, Energy transfer in lanthanide upconversion studies for extended optical applications, *Chem. Soc. Rev.* 44 (2015) 1608–1634.
 - [53] S.E. Habas, H. Lee, V. Radmilovic, G.A. Somorjai, P. Yang, Shaping binary metal nanocrystals through epitaxial seeded growth, *Nat. Mater.* 6 (2007) 692–697.
 - [54] Y.F. Chen, E. Johnson, X.G. Peng, Formation of monodisperse and shape-controlled MnO nanocrystals in non-injection synthesis: self-focusing via Ripening, *J. Am. Chem. Soc.* 129 (2007) 10937–10947.
 - [55] J. Thessing, J.H. Qian, H.Y. Chen, N. Pradhan, X.G. Peng, Interparticle influence on size/size distribution evolution of nanocrystals, *J. Am. Chem. Soc.* 129 (2007) 2736–2737.
 - [56] Z. Wang, Z. Li, A. Kornowski, X. Ma, A. Myalitsin, A. Mews, Solution-liquid-solid synthesis of semiconductor nanowires using clusters as single-source precursors, *Small* 7 (2011) 2464–2468.
 - [57] Y. Zhang, G.S. Hong, Y.J. Zhang, G.C. Chen, F. Li, H.J. Dai, Q.B. Wang, Ag₂S quantum dot: a bright and biocompatible fluorescent nanoprobe in the second near-infrared window, *ACS Nano* 6 (2012) 3695–3702.
 - [58] B. del Rosal, A. Pérez-Delgado, M. Misiak, A. Bednarkiewicz, A.S. Vanetsev, Y. Orlovskii, D.J. Jovanović, M.D. Dramićanin, U. Rocha, K. Uppendra Kumar, C. Jacinto, E. Navarro, E. Martín Rodríguez, M. Pedroni, A. Speghini, G.A. Hirata, I.R. Martín, D. Jaque, Neodymium-doped nanoparticles for infrared fluorescence bioimaging: the role of the host, *J. Appl. Phys.* 118 (2015), 143104.
 - [59] J.Y. Huang, Y. Hou, C.Y. Liu, L.H. Jing, T.C. Ma, X.D. Sun, M.Y. Gao, Chemical spacer design for engineering the relaxometric properties of core-shell structured rare earth nanoparticles, *Chem. Mater.* 27 (2015) 7918–7925.
 - [60] L. Wen, L. Chen, S. Zheng, J. Zeng, G. Duan, Y. Wang, G. Wang, Z. Chai, Z. Li, M. Gao, Ultrasmall biocompatible WO_{3-x} nanodots for multi-modality imaging and combined therapy of cancers, *Adv. Mater.* 28 (2016) 5072–5079.
 - [61] L.L. Li, R. Zhang, L. Yin, K. Zheng, W. Qin, P.R. Selvin, Y. Lu, Biomimetic surface engineering of lanthanide-doped upconversion nanoparticles as versatile bioprobes, *Angew. Chem. Int. Ed.* 51 (2012) 6121–6125.
 - [62] W.T. Al-Jamal, K. Kostarelos, Liposomes: from a clinically established drug delivery system to a nanoparticle platform for theranostic nanomedicine, *Acc. Chem. Res.* 44 (2011) 1094–1104.
 - [63] K.W. Ferrara, M.A. Borden, H. Zhang, Lipid-shelled vehicles: engineering for ultrasound molecular imaging and drug delivery, *Acc. Chem. Res.* 42 (2009) 881–892.
 - [64] L. Ye, K.T. Yong, L.W. Liu, I. Roy, R. Hu, J. Zhu, H.X. Cai, W.C. Law, J.W. Liu, K. Wang, J. Liu, Y.Q. Liu, Y.Z. Hu, X.H. Zhang, M.T. Swihart, P.N. Prasad, A pilot study in non-human primates shows no adverse response to intravenous injection of quantum dots, *Nat. Nanotechnol.* 7 (2012) 453–458.
 - [65] D.R. Coman, W.F. Sheldon, The significance of hyperemia around tumor implants, *Am. J. Pathol.* 22 (1946) 821–831.
 - [66] E. Carrasco, B. del Rosal, F. Sanz-Rodríguez, Á.J. de la Fuente, P.H. Gonzalez, U. Rocha, K.U. Kumar, C. Jacinto, J.G. Solé, D. Jaque, Intratumoral thermal reading during photo-thermal therapy by multifunctional fluorescent nanoparticles, *Adv. Funct. Mater.* 25 (2015) 615–626.
 - [67] X. Jiang, S. Zhang, F. Ren, L. Chen, J. Zeng, M. Zhu, Z. Cheng, M. Gao, Z. Li, Ultrasmall magnetic CuFeSe₂ ternary nanocrystals for multimodal imaging guided photothermal therapy of cancer, *ACS Nano* 11 (2017) 5633–5645.